Angewandte Chemie International Edition

Angewandte International Edition Chemie

How to cite: *Angew. Chem. Int. Ed.* **2026**, e5417029
doi.org/10.1002/anie.5417029

RESEARCH ARTICLE Hot Paper

A Polyzwitterionic "Ion-Sponge" Interphase via In Situ Self-Polymerization for Ultradurable Zinc Batteries

Lei Zhang[1,3] | Yunlong Zhang[1,2] | Yixu Wang[4] | Bo Zhang[5] | Mengyao Li[4] | Lan Yang[4] | Qian Wang[3,5] | Haiqi Gao[4] | Zhong Jin[3] | Shi Wang[2,3]

[1]School of Materials and Chemical Engineering, Chuzhou University, Chuzhou, China | [2]State Key Laboratory of Flexible Electronics (LoFE) & Institute of Advanced Materials (IAM), School of Chemistry and Life Sciences, Nanjing University of Posts & Telecommunications, Nanjing, Jiangsu, China | [3]State Key Laboratory of Coordination Chemistry, MOE Key Laboratory of Mesoscopic Chemistry, MOE Key Laboratory of High Performance Polymer Materials and Technology, Jiangsu Key Laboratory of Green Energy Catalysis and Intelligent Chemical Engineering, Suzhou Key Laboratory of Green Intelligent Manufacturing of New Energy Materials and Devices, Tianchang New Materials and Energy Technologies Research Center, Institute of Green Chemistry and Engineering, School of Chemistry and Chemical Engineering, Nanjing University, Nanjing, Jiangsu, China | [4]College of Chemistry, Xinjiang University (XJU), Ürümqi, China | [5]College of Materials Science and Engineering, Taiyuan University of Technology, Taiyuan, China

Correspondence: Qian Wang (qianwang0825@pku.edu.cn) | Haiqi Gao (gaohq@xju.edu.cn) | Zhong Jin (zhongjin@nju.edu.cn) | Shi Wang (iamshiwang@njupt.edu.cn)

Received: 16 June 2026 | **Revised:** 12 July 2026 | **Accepted:** 27 July 2026

Keywords: aqueous zinc batteries | hybrid SEI | in situ interface self-polymerization | polyzwitterion | solvation regulation

ABSTRACT

Aqueous zinc batteries hold great potential for grid storage applications; however, their practical deployment is severely limited by parasitic side reactions and uncontrollable dendrite formation. Herein, we design a polyzwitterionic "ion-sponge" interphase via an in-situ self-polymerization strategy. Specifically, under electric-field induction, zwitterion monomers polymerize into an ultrathin polyzwitterion layer that electrostatically enriches anions (OTf^-, SO_4^{2-}) and excludes water at the interface. This unique microenvironment enables the in-situ reductive conversion of anions into ZnF_2 and ZnS. The resulting polyzwitterion–ZnF_2/ZnS hybrid SEI enhances both the uniformity of Zn^{2+} deposition and the Zn^{2+} migration rate. The interfacial Zn^{2+} diffusion coefficient reaches 1.9×10^{-4} cm^2 s^{-1} (100 times higher than the bulk). Consequently, Zn||Zn symmetric cells stably cycle for over 1000 h at 5 mA cm^{-2} and 5 mAh cm^{-2}, and also for over 5500 h at −20 °C. Full cells with V_2O_5 cathode achieve a high average capacity of 339 mAh g^{-1} and 99.9% Coulombic efficiency over 1900 cycles, along with stable low-temperature operation. This polyzwitterionic "ion-sponge" interphase concept provides in-depth insights into interfacial ion transport regulation for high-performance aqueous zinc batteries.

1 | Introduction

Rechargeable aqueous zinc-ion batteries (RAZBs) have emerged as attractive alternatives for grid-scale energy storage systems, owing to their cost-effectiveness, inherent safety, and high theoretical capacity of metallic zinc (820 mAh g^{-1} and 5855 mAh cm^{-3}) in mildly acidic electrolytes [1–7]. Nevertheless, the practical deployment of RAZBs is hampered by interfacial instability and compatibility issues, which stem from the high electrochemical reactivity of zinc anodes and their propensity for spontaneous side reactions in aqueous media [8–12]. These challenges manifest as persistent

Lei Zhang, Yunlong Zhang, Yixu Wang, and Bo Zhang contributed equally to this study.

hydrogen evolution, zinc corrosion, and dendrite formation at the electrode–electrolyte interface, collectively undermining the cycling reversibility and operational durability of RAZBs [13, 14].

Substantial efforts have been devoted to addressing these issues, including electrolyte engineering via functional additives [15–17], design of hydrogel or solid-state polymer electrolytes [18–20], and construction of artificial interphases [21, 22]. Among these, the construction of an artificial SEI is particularly prevalent for isolating the Zn anode from the aqueous electrolyte [23, 24]. Compared with inorganic or small-molecule organic interphase layers [25–27], polymer interphase layers offer the advantages of easy processability, high designability, and excellent adhesion to electrodes, making them highly promising materials for constructing artificial SEIs [6, 28]. Consequently, various functional polymers have been applied to stabilize Zn anodes, such as polyimide [29], polyacrylamide [24], polyamide [30]. During battery cycling, the Zn anode surface is subjected to volumetric stress generated by the reduction of Zn^{2+} to metallic Zn, as well as local stress variations caused by the reduction and plating of Zn^{2+}. This requires polymer interphase layers to combine high mechanical strength with fast Zn^{2+} transport capability to achieve interfacial stability of the Zn anode [31]. However, achieving this combination is inherently challenging: thick polymer layers afford sufficient modulus but impede Zn^{2+} migration and induce high polarization [32, 33], whereas thin layers, though potentially improving ionic kinetics, lack the ionic functionality to regulate uniform Zn^{2+} deposition and are prone to cracking under high-rate or deep-cycling conditions [34, 35]. Even hybrid designs, such as polyacrylamide-inorganic SEI, [24] face unresolved issues regarding thickness control and long-term stability of the inorganic components [36]. Therefore, developing an ultrathin polymer interphase that reconciles high mechanical strength with fast Zn^{2+} transport remains a critical challenge.

Herein, we report a conceptually different approach based on interfacial polymerization: a zwitterion-modulated electrolyte that not only regulates the bulk solvation structure from the source, but more importantly, enables the in-situ self-polymerization of zwitterionic monomers at the interface to form a unique polyzwitterionic "ion-sponge" interphase. This interphase electrostatically enriches OTf^- and SO_4^{2-} at the Zn surface while excluding water molecules. Such an anion-enriched, water-depleted interface promotes the localized decomposition of anions at the interface, simultaneously forming inorganic interfacial components. Ultimately, this yields an ultrathin (~40–80 nm) and high-strength (up to 44.7 GPa) polyzwitterionic/inorganic hybrid SEI composed of ZnF_2/ZnS, which combines the flexibility of the polymer and its rapid Zn^{2+} diffusion pathways with the high modulus of the fluoride/sulfide. Consequently, Zn||Zn symmetric cells sustain stable cycling for over 1000 h at 5 mA cm^{-2} and 5 mAh cm^{-2} and can stably cycle for over 5500 h at −20°C, outperforming most previously reported systems. Furthermore, full cells also exhibit significantly enhanced cycling stability at room temperature and −20°C, underscoring the practical potential of this hybrid interphase design.

2 | Results and Discussion

2.1 | Solvation Structure Modulation and Interfacial Polymerization Verification

In this study, we prepared four different electrolytes: 2 M $Zn(OTf)_2$, 0.2 M Zw in 2 M $Zn(OTf)_2$, 2 M $Zn(OTf)_2$ with 0.2 M $ZnSO_4$, and 0.2 M Zwitterionic (Zw) in 2 M $Zn(OTf)_2$ with 0.2 M $ZnSO_4$. We conducted an in-depth investigation into the effects of Zw and the types of zinc salts on the performance of the electrolytes. For the sake of convenience, these electrolyte systems are referred to as $Zn(OTf)_2$, Zw-$Zn(OTf)_2$, $Zn(OTf)_2$-$ZnSO_4$, and Zw-$Zn(OTf)_2$-$ZnSO_4$, respectively. Figure 1 shows the solvation structure evolution and interface regulation principle of $Zn(OTf)_2$, $Zn(OTf)_2$-$ZnSO_4$, and Zw-$Zn(OTf)_2$-$ZnSO_4$ electrolyte. Specifically, Figure 1a shows that the Zn^{2+} solvated with 5 water molecules and 1 OTf^- anion in the $Zn(OTf)_2$ electrolyte easily causes hydrogen evolution corrosion and uneven dendrite growth on the anode surface. Upon the introduction of zinc sulfate, the content of water molecules in the solvation shell of Zn^{2+} is further reduced (Figure 1b). Although this can mitigate side reactions such as hydrogen evolution corrosion, it still cannot be effectively avoided. Figure 1c demonstrates that adding zwitterionic monomers further reduces the coordinated water in the solvation structure. These monomers can self-polymerize on the anode surface under the action of zinc ions. Our research revealed that the Zw-$Zn(OTf)_2$-$ZnSO_4$ electrolyte facilitates the formation of unique organic-inorganic solid electrolyte interphase (SEI) film components, significantly enhancing battery performance. The formation process of the polymer-inorganic solid electrolyte interphase (SEI) was explored through a combination of theoretical computations and experimental investigations. Zw molecules exhibit strong binding affinity toward Zn species. When Zn species are adsorbed, they can abstract electrons from the carbonyl moiety, accompanied by an intensified delocalization of conjugated electrons. This leads to the formation of a free radical intermediate from the unsaturated C═C bond, which then triggers chain propagation during electrochemical reduction (as depicted in Figure 1d and Figure S1). The free energies associated with this polymerization reaction were calculated, revealing that the reaction involving Zn^{2+} exhibits a lower free energy change (Table S1 and Figure S2), suggesting that the polymerization process is thermodynamically favored in the presence of a Zn^{2+} catalyst. Based on the in situ Raman spectroscopy data (Figure 2a), a characteristic peak corresponding to Zw can be discerned at ~1625 cm^{-1}, which is attributed to the C ═C stretching vibration. As the plating duration increases, the intensity of this peak, associated with C═C stretching, progressively diminishes and eventually vanishes. These findings provide additional evidence that the Zw monomer undergoes gradual polymerization to form PZw, ultimately leading to the deposition of a polymer layer on the surface of Zn. Notably, this polymerization is predominantly interfacial rather than bulk, as evidenced by the preferential adsorption of zwitterions on Zn, the consumption of C═C bonds at the interface, and so on (see the following discussion). For the Zw-$Zn(OTf)_2$-$ZnSO_4$ electrolyte system, in situ Raman characterization revealed a significant blue shift of characteristic peaks in the 1030–1050 cm^{-1} range during 23 consecutive charge/discharge cycles (Figure 2b). This

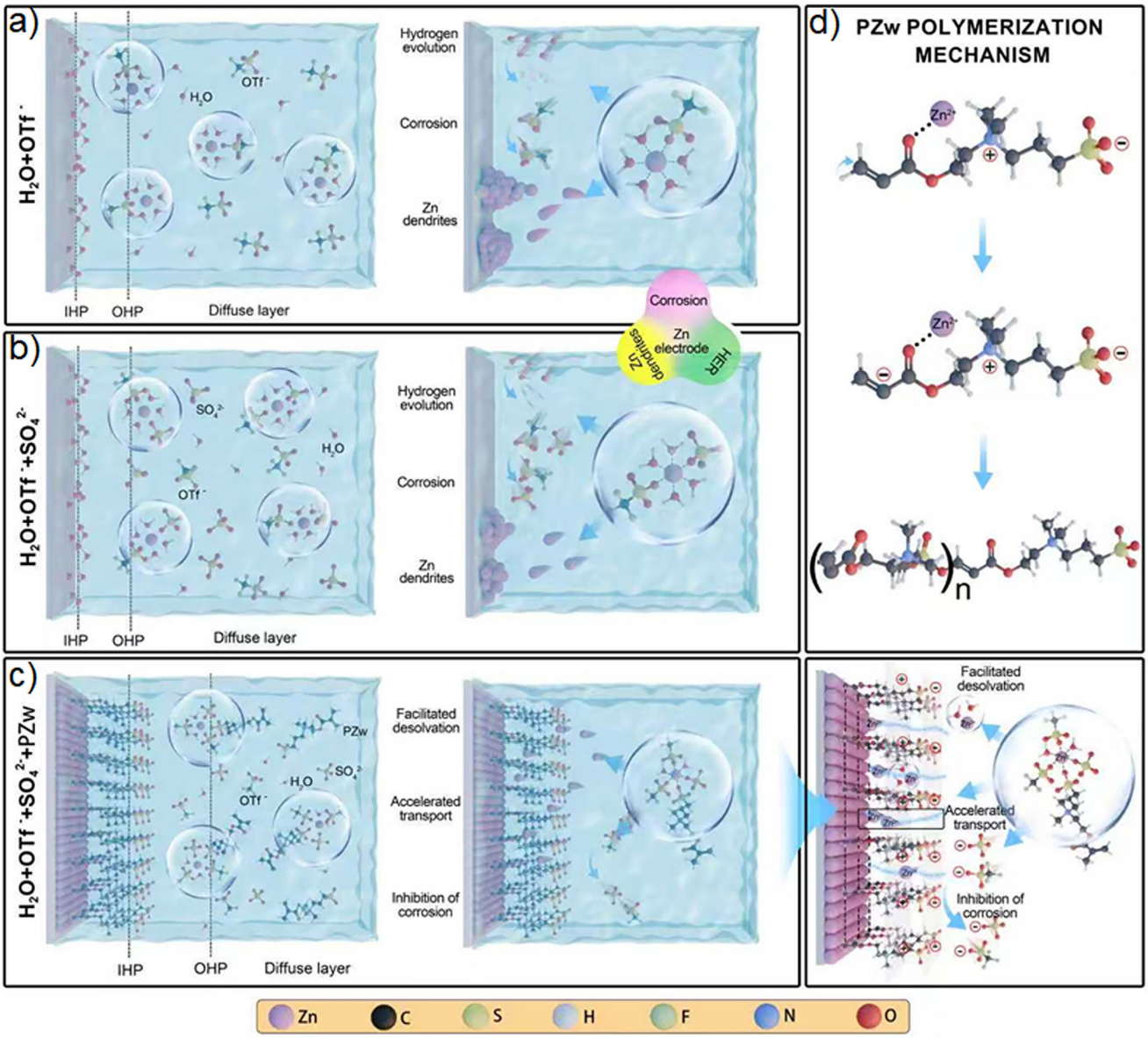

FIGURE 1 | Interfacial regulation mechanism of Zinc-based batteries: The solvation structure evolution and interface regulation principle of (a) $Zn(OTf)_2$, (b) $Zn(OTf)_2$-$ZnSO_4$, and (c) Zw-$Zn(OTf)_2$-$ZnSO_4$ electrolytes.

phenomenon indicates an increase in contact and aggregated ion pairs within the zinc ion solvation structure. Following zwitterion polymerization, the unique polymer chains formed at the interface effectively weaken water-zinc ion coordination, resulting in an anion-enriched solvent shell around zinc ions. As shown in Figure 2c, DFT calculations reveal that the binding energy between Zn^{2+} and Zw is higher than that between Zn^{2+} and H_2O, indicating that the introduction of Zw not only facilitates the dissociation of the zinc salt but also provides additional sites for Zn^{2+} transport. More importantly, Zw can enter the solvation shell of Zn^{2+} and thus modulate its solvation structure. Moreover, the binding energy between Zn^{2+} and SO_4^{2-} is significantly higher than that between Zn^{2+} and OTf^-, thereby ensuring the effective entry of SO_4^{2-} into the solvation shell of zinc ions even under low-concentration conditions. Additionally, the binding energy of Zn^{2+} with OTf^- is −15.15 eV, which lies between that of Zn^{2+} with SO_4^{2-} (−26.83 eV) and Zn^{2+} with Zw (−10.76 eV). This correspondingly facilitates the incorporation of an appropriate amount of OTf^- into the zinc ion solvation shell.

Molecular electrostatic potential (MEP) maps reveal that the zwitterionic compound exhibits a moderately negative electrostatic potential near its negatively charged group and a positive potential near its quaternary ammonium group (Figure 2d). This unique charge distribution enables the cationic part of the zwitterion to preferentially adsorb onto the negatively charged anode surface, while the anionic part provides potential sites for Zn^{2+} migration. The MEP map of the OTf^- anion shows a more negative electrostatic potential around its sulfonate group ($-SO_3^-$, Figure 2e), which serves as the primary interaction site for Zn^{2+}. For the SO_4^{2-} anion, the MEP map indicates that the oxygen atoms bear a more negative electrostatic potential and likewise

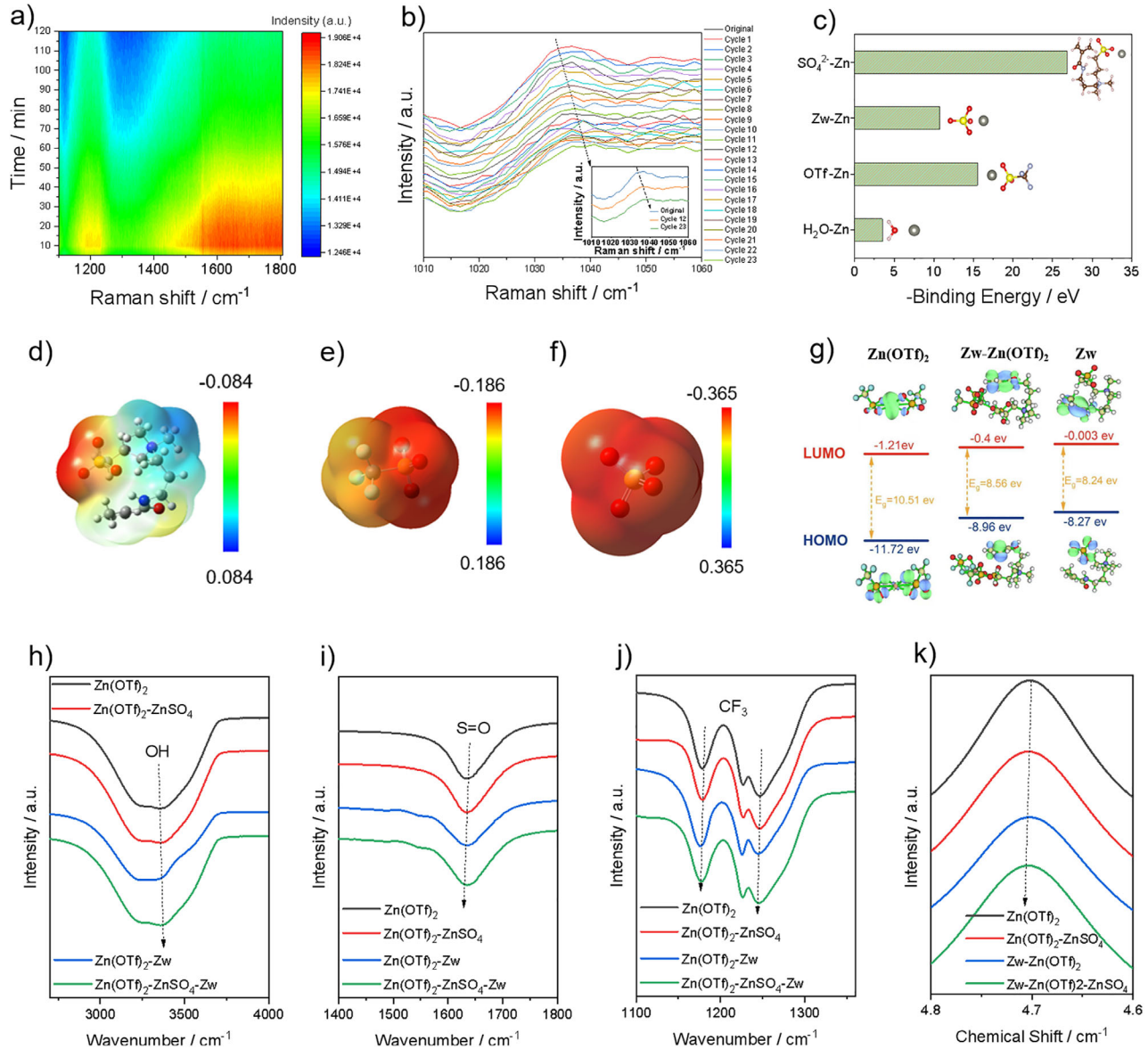

FIGURE 2 | Integration of spectroscopic and theoretical analyses to reveal electrolyte chemistry and zinc anode interfacial evolution: (a, b) In situ Raman spectra of the zinc anode surface at various plating time. (c) Binding energy of Zn^{2+} with different compositions in electrolyte. Molecular electrostatic potential maps of (d) Zw, (e) OTf^- and (f) SO_4^{2-}. (g) HOMO and LUMO energy level of various compositions in electrolyte. (h–j) IR spectra of different electrolytes. (k) ^1H NMR of different electrolytes.

act as the main Zn^{2+} binding sites (Figure 2f). Notably, the negative electrostatic potential values in the negatively charged regions of OTf^- (i.e., $-SO_3^-$) and SO_4^{2-} (i.e., O atoms) are more negative than that of the anionic part of the zwitterion. This implies that the electrostatic interaction of Zn^{2+} with OTf^- and SO_4^{2-} is stronger than that with the zwitterion. This trend is fully consistent with the calculated binding energies (Zn^{2+}–SO_4^{2-}: −26.83 eV, Zn^{2+}–OTf^-: −15.15 eV, Zn^{2+}–Zw: −10.76 eV): the stronger interactions enable OTf^- and SO_4^{2-} to stably participate in the solvation shell of Zn^{2+} but also render them less prone to dissociation from the shell. In contrast, the weaker interaction between Zn^{2+} and the zwitterion favors both the dissociation of the zinc salt and the rapid release of Zn^{2+} during transport.

As shown in Figure 2g, introducing the zwitterion raises the LUMO level, but more importantly, the HOMO level of Zw-$Zn(OTf)_2$ increases from −11.72 to −8.96 eV, indicating a stronger electron-donating capability. This promotes interaction with the Zn anode and facilitates localized decomposition of OTf^- at the interface, leading to greater formation of typical inorganic species like ZnF_2. Meanwhile, the bandgap decreases from 10.51 to 8.56 eV, easing electronic transitions and further supporting the reduction process.

The changes in the solvation structure of zinc ions were further verified by infrared and nuclear magnetic resonance characterizations. As shown in Figure 2h, the characteristic OH peak from IR spectra exhibits a distinct blue shift upon adding $ZnSO_4$ or Zw to 2 M $Zn(OTf)_2$, and the shift is more pronounced when both Zw and $ZnSO_4$ are introduced. Furthermore, the characteristic peaks of S═O (Figure 2i), S–O (Figure S3), and CF_3 (Figure 2j) in OTf^- show a red shift with the addition of $ZnSO_4$ or Zw, and

the shift is enhanced when both are present. A consistent trend is observed for the OH peak in ^{1}H NMR spectra (Figure 2k). These phenomena can be attributed to the stronger binding of Zn^{2+} to OTf^-, SO_4^{2-} and Zw compared to H_2O, which drives the anions and Zw into the Zn^{2+} solvation shell and effectively regulates the solvation structure.

2.2 | Interfacial Coordination Environment and Ion Transport Kinetics

To further clarify the regulatory mechanism of the introduction of $ZnSO_4$ and zwitterion on the solvation structure of the system, molecular dynamics (MD) simulations were employed. Figure S4a and S4b present the MD snapshot and the corresponding radial distribution functions (RDFs) for a 2 M $Zn(OTf)_2$ solution, respectively. RDF analysis reveals that each Zn^{2+} ion is coordinated by 4.78 water molecules and 1.22 OTF^- anion, forming a six-coordination structure. The ion diffusion coefficients as a function of time are shown in Figure S4c. The diffusion coefficient of OTF^- (2.13×10^{-6} cm^2 s^{-1}) is significantly higher than that of Zn^{2+} (1.28×10^{-6} cm^2 s^{-1}). According to the RDF results in Figure S4d, Zn^{2+} primarily coordinates with the oxygen atoms, rather than the sulfur atom, of the OTF^- anions in the 2 M $Zn(OTf)_2$ solution.

Upon the addition of 0.2 M $ZnSO_4$ to the 2 M $Zn(OTf)_2$ solution, Figure S5a,b demonstrate that the coordination number (CN) of Zn^{2+} with water decreases to 4.45. Within the first solvation shell, besides a small number of OTF^- anions (1.34), a minor amount of SO_4^{2-} anions (0.21) also participates in the coordination. In terms of diffusivity, OTf^- remains the dominant species (Figure S5c). Specifically, the diffusion coefficient of OTf^-, Zn^{2+} and SO_4^{2-} are 2.41×10^{-6}, 1.78×10^{-6} and 0.98×10^{-6} cm^2 s^{-1}, respectively. Furthermore, for the predominant anion OTF^-, its inner-sphere coordination to Zn^{2+} still involves the oxygen atoms, not the sulfur atom (Figure S5d).

The introduction of Zw induces further modifications to the Zn^{2+} solvation structure. Specifically, the CN of Zn^{2+} with water shows a further decrease (Figure 3a,b; 4.19), while the number of coordinating OTF^- (1.48) and SO_4^{2-} (0.25) anions increases. It is found that the OTF^- diffusion still predominates (1.36×10^{-6} cm^2 s^{-1}, Figure 3c), and the Zn^{2+} diffusion coefficient is slightly decreased (0.91×10^{-6} cm^2 s^{-1}). This is most likely because, in the bulk phase, the zwitterions participate in coordinating with Zn^{2+} ions, thereby raising the desolvation energy barrier of Zn^{2+}.

The migration behavior of ions at the interface is of particular importance. Based on the binding energies of the zwitterion and water molecules on different crystal facets, the (002) facet is identified as the most favorably exposed plane (to be discussed in detail later). Consequently, we further investigated the solvation structure and migration dynamics of ions at the interface of the (002) facet. Figure 3d shows a representative MD snapshot of the interfacial region. The RDF in Figure 3e indicates a drastic reduction in the number of coordinating water molecules around Zn^{2+} at the interface to merely 1.98, while the CN of OTF^- increases substantially to 1.71. The CN of SO_4^{2-} also rises to 0.33. Concurrently, the Zn^{2+} diffusion coefficient at the interface increases further, approaching that of OTf^- (Figure 3f). The diffusion coefficient of OTf^-, Zn^{2+} and SO42$^-$ are 1.92×10^{-4}, 1.9×10^{-4} and 1.93×10^{-4} cm^2 s^{-1}, respectively. A direct comparison of the Zn^{2+} diffusion coefficients in the 2 M $Zn(OTf)_2$, $Zn(OTf)_2$-$ZnSO_4$, and Zw-$Zn(OTf)_2$-$ZnSO_4$ systems is presented in Figure 3g. The results clearly demonstrate that the introduction of the polyzwitterion interface leads to a remarkable enhancement in Zn^{2+} diffusivity. This suggests that at the interface, after self-polymerization, the cationic groups of the zwitterions further effectively immobilize the anions via electrostatic interactions, thereby enabling uniform and rapid Zn^{2+} deposition guided by the anions. The interfacial RDFs provide further evidence that within the innermost interfacial layer, Zn^{2+} ions preferentially adsorb onto the surface of the (002) facet, with noticeable ion accumulation observed near the Zn crystal plane (Figure 3i).

Furthermore, by comparing the RDFs for water molecules (Figure 3h) and OTf^- anions (Figure S6) within the Zn^{2+} solvation shell across different systems, an intuitive trend is observed: the sequential introduction of $ZnSO_4$ and Zw leads to a continuous decrease in the number of coordinating water molecules and a concomitant increase in the CN of OTf^-. This effect is particularly pronounced at the interface, where the CN of water drops sharply while the CN of OTf^- rises significantly. Figure 3j visualizes the dynamic migration of Zn^{2+} from the bulk electrolyte to the Zn (002) interface. As Zn^{2+} approaches the electrode surface, its coordination with water molecules progressively weakens, while interactions with the oxygen atoms of OTf^- and SO_4^{2-}, as well as with the negatively charged sulfonate group of the zwitterion, gradually intensify, which indicates the polymer-based interface can act as a polyzwitterionic "ion-sponge" interphase. This transition from water-dominated to anion-enriched solvation at the interface directly underpins the enhanced Zn^{2+} diffusivity and uniform deposition.

2.3 | Electrochemical Performance, Interfacial Evolution, and Dendrite Suppression

Figure 4a shows the EIS of various electrolytes, it is seen that Zw-$Zn(OTf)_2$-$ZnSO_4$ shows lower bulk resistance than other ones, this can be attributed to the special structure of Zw that provide Zn^{2+} transport route. The illustration in Figure 4a also shows that after the sample was soaked in Zw-$Zn(OTf)_2$-$ZnSO_4$ solution, the zinc surface was covered with a uniform and thin polymer film. In contrast, the control sample did not show this (Figure S7). Contact angle measurements further demonstrate that the zinc surface modified with Zw-$Zn(OTf)_2$-$ZnSO_4$ exhibits enhanced hydrophilicity, with a contact angle of 18.7°, whereas the surfaces modified with $Zn(OTf)_2$ and $Zn(OTf)_2$-$ZnSO_4$ show contact angles of 69.1° (Figure 4b) and 41.9° (Figure S8), respectively. This improvement is attributed to the adsorption of the cationic hydrophobic ends of the zwitterionic polymer layer onto the zinc anode surface, while the anionic hydrophilic ends remain exposed to the exterior. The hydrophilic layer can facilitate uniform adsorption of Zn^{2+}, provides abundant nucleation sites, reduces the nucleation overpotential, and promotes two-dimensional diffusion, thereby guiding lateral and dense zinc growth and suppressing dendrite formation. The above conclusion is further verified through a series of electrochemical characterizations. Typically, Figure 4c presents the linear sweep voltammetry (LSV) curves of Zn||SS cells assembled with various

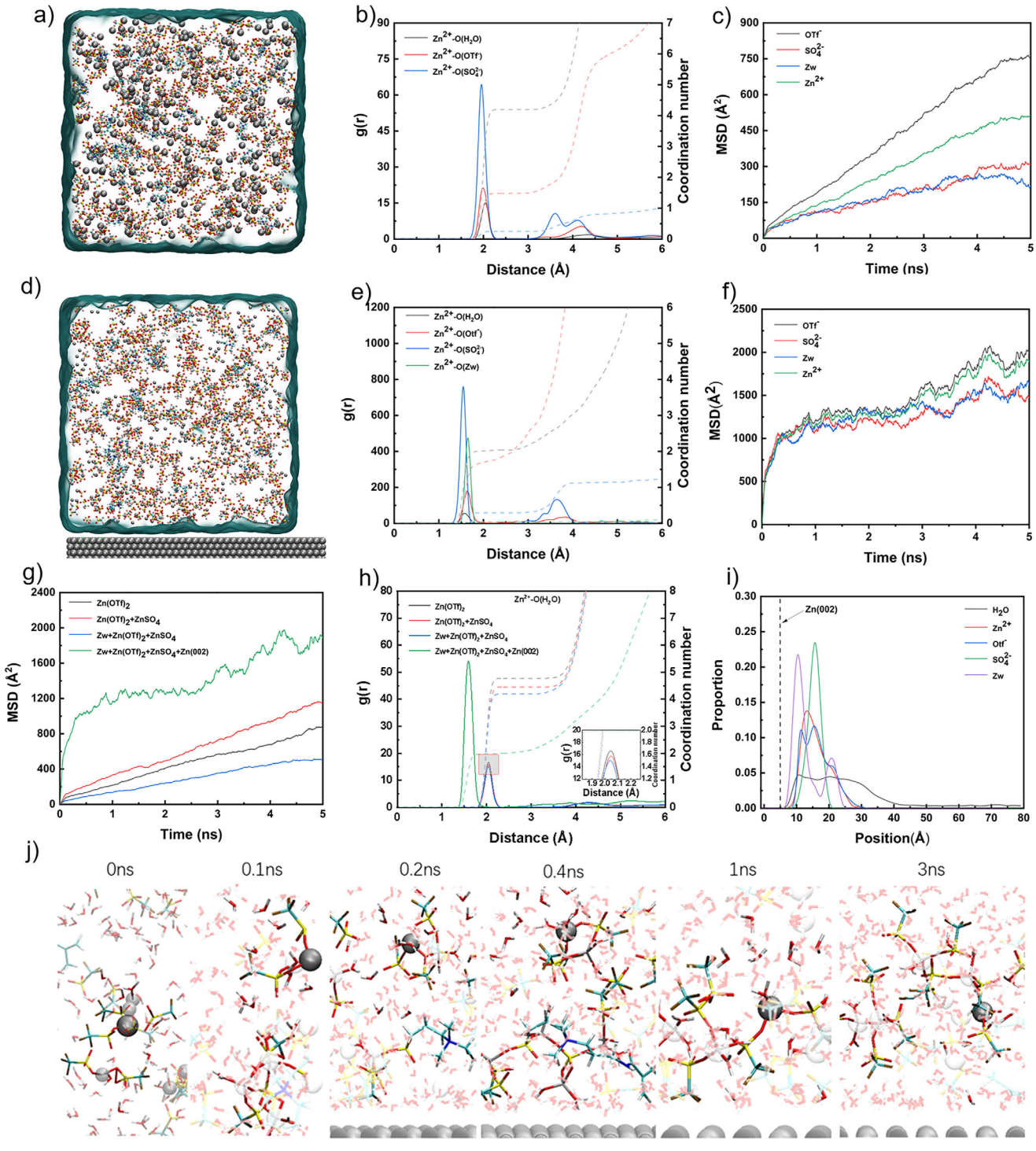

FIGURE 3 | MD simulations of Zn^{2+} coordination, diffusion, and interfacial transport in the optimal electrolyte: (a) Snapshot of the equilibrated configuration from MD simulations of the optimal electrolyte (Zw-Zn(OTf)$_2$-ZnSO$_4$). (b) Coordination number and radial distribution function of Zn^{2+} in the optimal electrolyte and (c) corresponding diffusion coefficients of different ions and molecules. (d) Snapshot of the equilibrated configuration from MD simulations at the (002) interface. (e) Coordination number and radial distribution function of Zn^{2+} in the optimal electrolyte near the interface, and (f) diffusion coefficients of different ions and molecules at the interface. (g) Comparison of zinc ion diffusion coefficients across different electrolyte systems based on kinetic simulations, along with the zinc ion diffusion coefficient in the optimal electrolyte at the interface. (h) Coordination environment and radial distribution function of zinc ions with water in different electrolyte systems and in the interfacial layer of the optimal electrolyte. (i) Distribution of different ions and molecules in the optimal electrolyte at the (002) interface. (j) Kinetic simulation of zinc-ion transport from the bulk phase to the interface.

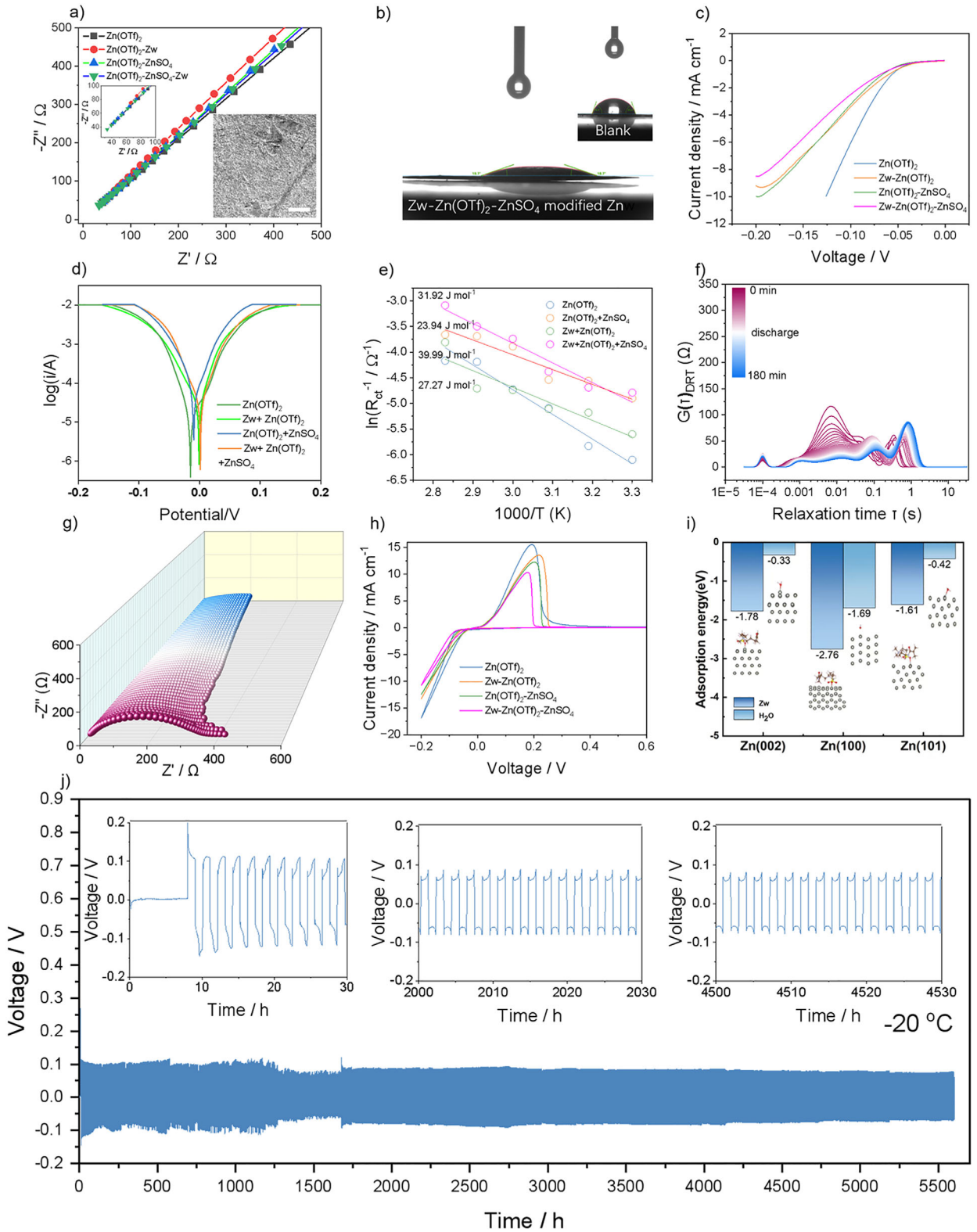

FIGURE 4 | Electrochemical properties and interfacial kinetics of the optimal electrolyte: (a) Ionic conductivity of various electrolytes (the inset shows the SEM image of modified Zn surface using Zw-Zn(OTf)$_2$-ZnSO$_4$, Scale bar: 10 μm). (b) Contact angles of modified Zn. (c) LSV curves of various electrolytes. (d) Tafel curves of various electrolytes. (e) Relationship of R_{ct} versus T in various electrolytes. (f) Evolution of distribution of relaxation times (DRT) patterns, obtained from the (g) in situ EIS data. (h) Cyclic voltammograms of Zn||Cu cells in various electrolytes (scanning rate: 5 mV s^{-1}). (i) The differences in adsorption energies of water and Zw on different crystal faces of zinc. (j) Cycle performance of Zn||Zn cell using Zw-Zn(OTf)$_2$-ZnSO$_4$ at −20°C.

electrolyte samples. The onset potential for the hydrogen evolution reaction (HER) in the Zn|Zw-Zn(OTf)$_2$-ZnSO$_4$|SS system is lower compared to Zn|Zn(OTf)$_2$|SS, Zn|Zw-Zn(OTf)$_2$|SS, and Zn|Zn(OTf)$_2$-ZnSO$_4$|SS configurations. This phenomenon can be attributed to the reduced content of solvated water around zinc ions in the Zw-Zn(OTf)$_2$-ZnSO$_4$ electrolyte, coupled with the highly interconnected hydrogen bond network within the interfacial polymer gel components, which effectively suppresses the reactivity of H_2O. Concurrently, the LSV curves (Figure S9) demonstrate a significant increase in the oxygen evolution reaction (OER) potential alongside reduced current response for Zn||SS cells based on Zw-Zn(OTf)$_2$-ZnSO$_4$. These observations indicate that the electrolyte effectively extends the electrochemical stability window (ESW) while inhibiting water splitting at both cathode and anode interfaces.

To evaluate the corrosion rate of zinc, Tafel tests were conducted to measure the corrosion current of corresponding cells. As shown in Figure 4d, the corrosion current for the zinc anode in Zw-Zn(OTf)$_2$-ZnSO$_4$ electrolyte is 0.24 mA cm^{-2}, significantly lower than the values of other electrolyte, such as 0.51 mA cm^{-2} observed for Zw-Zn(OTf)$_2$. The desolvation energy in Zw-Zn(OTf)$_2$-ZnSO$_4$ electrolyte was calculated as 31.92 kJ·mol^{-1}. Although this value is higher than those of other reference samples (Figure 4e), the Zw-Zn(OTf)$_2$-ZnSO$_4$ system exhibits the lowest interfacial resistance across the entire temperature range (Figure S10). DRT patterns (Figure 4f, with corresponding Nyquist plots shown in Figure 4g) further demonstrate that during the discharge process, the peak intensities associated with bulk zinc-ion transport and interfacial charge transfer are reduced, indicating that the zwitterion have enhanced the overall conductivity. The relatively higher desolvation energy may stem from the participation of certain zwitterionic species in the coordination environment as solvent components. Notably, this desolvation energy remains substantially lower than the 61.4 kJ·mol^{-1} reported for liquid electrolytes [37].

Dendrite formation during charge/discharge cycles represents a critical challenge for zinc-based batteries, closely associated with Zn nucleation and growth behavior. To investigate the Zn nucleus radius and density, cyclic voltammetry (CV) was employed to determine the nucleation overpotential (NOP) of Zn/Cu asymmetric cells. As depicted in Figure 4h, the NOP for Zn deposition on Cu foil in Zw-Zn(OTf)$_2$-ZnSO$_4$ electrolyte is higher than those observed in other electrolyte systems. This indicates that zinc anode cycled in Zw-Zn(OTf)$_2$-ZnSO$_4$ form smaller nuclear radii, promoting the formation of fine, uniformly distributed zinc particles during deposition. To further elucidate the Zn nucleation mechanism, chronoamperometry (CA) measurements were performed (Figure S11). In Zn(OTf)$_2$, Zw-Zn(OTf)$_2$, and Zn(OTf)$_2$-ZnSO$_4$ electrolytes, the Zn anodes exhibit rapid two-dimensional (2D) diffusion processes, with current values changing rapidly over time, suggesting uncontrolled growth of porous Zn deposits and consequent rapid expansion of specific surface area. In contrast, the Zw-Zn(OTf)$_2$-ZnSO$_4$ electrolyte suppresses the 2D diffusion process, transitioning directly to a stable three-dimensional (3D) diffusion regime with low constant current, indicating controlled evolution of Zn nuclei into uniform Zn layers. DFT calculations (Figure 4i) show that the zwitterion exhibits adsorption energies of −2.76, −1.78, and −1.61 eV on Zn (100), (002), and (101) planes, respectively. These values are all significantly more negative than those of water (−1.69, −0.33, −0.42 eV), indicating that the zwitterion preferentially adsorbs onto Zn surfaces by displacing interfacial water. The overly strong adsorption on Zn(100) (−2.76 eV) overpassivates this plane, nearly halting its perpendicular growth. The weakest adsorption on Zn(101) (−1.61 eV) provides limited protection, allowing the fastest growth along this direction. The moderate adsorption on Zn(002) (−1.78 eV) effectively replaces water without excessively suppressing growth. During competitive growth, the fastest growing Zn(101) plane is quickly encased and eliminated by slower growing neighbors; the nearly stagnant Zn(100) plane gradually loses out; and the moderately growing Zn(002) plane emerges as the dominant exposed facet, consistent with XRD results (Figure S12). Thus, the preferential Zn(002) exposure directly reflects the zwitterion's differential adsorption modulating the relative growth kinetics of Zn facets.

Symmetric Zn||Zn cells were further employed to assess the ability of different electrolytes to inhibit zinc dendrite formation. As shown in Figure 4j, even at −20°C, the Zn||Zn battery based on the optimal electrolyte can stably cycle for over 5500 h under a current density of 0.1 mA cm^{-2} and a capacity of 0.1 mAh cm^{-2}. Moreover, as shown in Figure 5a, the comparison of rate performance indicates that when the current density increased from 0.2 to 6 mA cm^{-2} at room temperature, the symmetric cells using Zn(OTf)$_2$ electrolyte experienced significant short-circuiting. While Zn(OTf)$_2$-ZnSO$_4$ electrolyte enabled relatively stable Zn plating/stripping at current densities ranging from 0.2 mA cm^{-2} to 8 mA cm^{-2}, short-circuiting occurred after 50 h of cycling at 1 mA cm^{-2}. The introduction of Zw significantly improved the rate capability and stability of symmetric zinc cells. Notably, the electrolyte containing both Zw and ZnSO$_4$ demonstrated not only superior rate performance but also exceptional long-term stability, maintaining extremely low overpotential for over 400 h of cycling. The cycling performance of Zn||Zn symmetric cells assembled with various electrolytes was further compared under elevated current density (5 mA cm^{-2}). As depicted in Figure 5b, the Zn|Zn(OTf)$_2$|Zn cell exhibited noticeable soft shorting after approximately 80 h of cycling. In contrast, the Zn|Zw-Zn(OTf)$_2$|Zn cell maintained stable operation until soft shorting occurred at ∼550 h. Notably, the Zn|Zw-Zn(OTf)$_2$-ZnSO$_4$|Zn cell demonstrated exceptional cycling stability exceeding 1100 h with a steady overpotential of ∼90 mV. These findings further validate the critical role of synergistic interaction between zwitterionic components and ZnSO$_4$ in stabilizing zinc anode performance.

Post-cycling morphological characterization of zinc anodes revealed distinct differences (Figure 5c–f). Compared to anodes cycled in Zn(OTf)$_2$, Zn(OTf)$_2$-ZnSO$_4$, and Zw-Zn(OTf)$_2$ electrolytes, the Zw-Zn(OTf)$_2$-ZnSO$_4$-based anode exhibited a dendrite-free surface with dense and uniform zinc deposition, corroborating results from chronoamperometry (CA) analysis. XRD characterization (Figure S12) further shows that after cycling with the Zw-Zn(OTf)$_2$-ZnSO$_4$ electrolyte, the Zn anode surface exhibits an I(002)/I(001) intensity ratio of 3.9, significantly higher than those obtained with Zn(OTf)$_2$-ZnSO$_4$ (2.3) and Zw-Zn(OTf)$_2$ (2.6). These results strongly indicate that the Zw-Zn(OTf)$_2$-ZnSO$_4$ electrolyte promotes preferential Zn deposition along the (002) plane, which is consistent with the theoretical calculations.

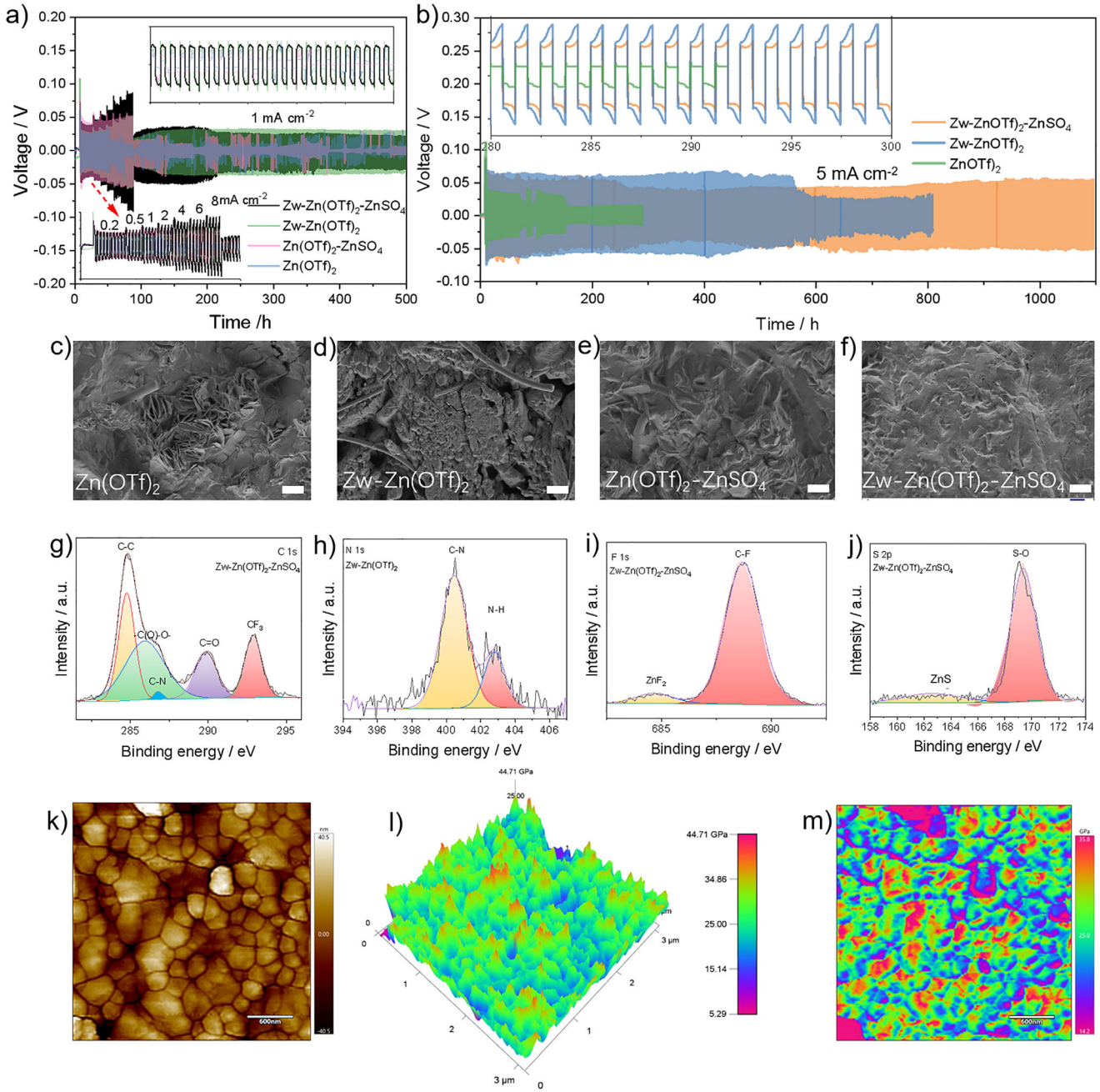

FIGURE 5 | Cycling stability, anode morphology, and interfacial composition of Zn anodes: (a) Rate performance of Zn||Zn symmetric cells in various electrolytes. (b) Long cycle performance of Zn||Zn symmetric cells in various electrolytes under current density of 5 mA cm^{-2}. SEM images of the cycled Zn surface using (c) $Zn(OTf)_2$, (d) Zw-$Zn(OTf)_2$, e) $Zn(OTf)_2$-$ZnSO_4$ and (f) Zw-$Zn(OTf)_2$-$ZnSO_4$. The scale bar is 10 μm. (g) C1s, (h) N 1S, (i) F 1s, and (j) S 2p of the Zn surface of cycled Zn||Zn cell using Zw-$Zn(OTf)_2$-M $ZnSO_4$. (k) Atomic force microscopy (AFM) topography image of SEI based on Zn||Zn using Zw-$Zn(OTf)_2$-M $ZnSO_4$. (l) 3D Young's modulus mapping of the hybrid SEI. (m) 2D modulus plane distribution of the SEI.

X-ray photoelectron spectroscopy (XPS) analysis revealed analogous carbon-based organic components on zinc surfaces cycled in all four electrolytes (Figure 5g and Figure S13a,d,j,k). However, zwitterion incorporation induced enrichment of organic nitrogen species in the solid electrolyte interphase (SEI) (Figure 5h). Significant differences were observed in inorganic components: the Zw-$Zn(OTf)_2$-$ZnSO_4$ electrolyte promoted formation of an SEI layer with elevated ZnF_2 content (Figure 5i, contrast samples in Figure S13b,e,h) and detectable ZnS (Figure 5j), whereas ZnS was absent in control samples (Figure S13c,f,i). These results confirm that the Zw-$Zn(OTf)_2$-$ZnSO_4$ formulation facilitates SEI formation with enhanced organic content and the inclusion of ZnF_2 and ZnS—critical compositional features underlying stable Zn||Zn cell performance. The mechanistic origin of this unique hybrid SEI lies in the anion-enriched, water-depleted interface created by the in situ polymerized polyzwitterion layer. The cationic quaternary ammonium groups of the polyzwitterion electrostatically adsorb and enrich OTf^- and SO_4^{2-} anions at the electrode/electrolyte interface, while simultaneously excluding water molecules from the immediate vicinity of the Zn surface.

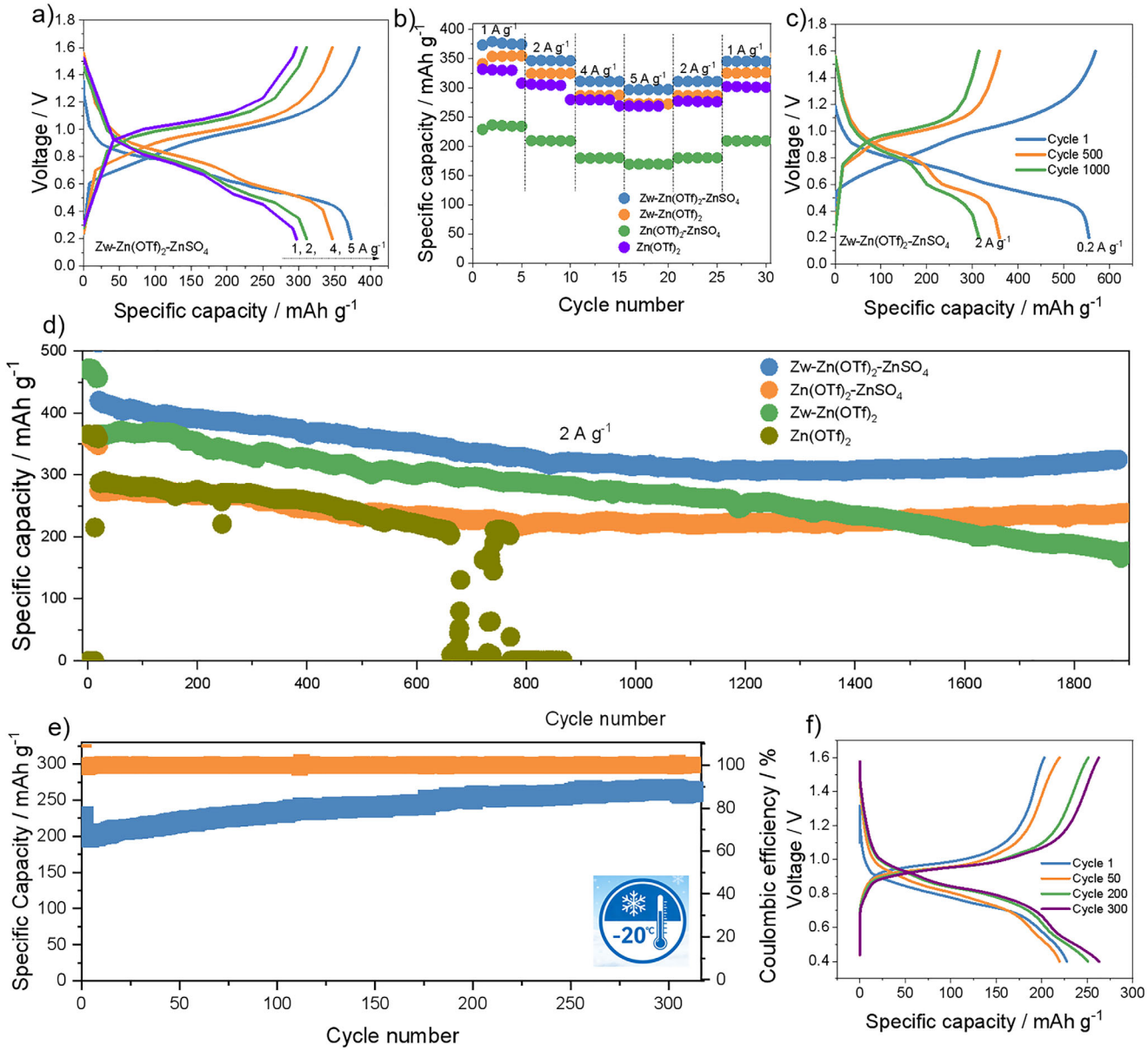

FIGURE 6 | Cell performance: (a) Charging/discharging curves of Zn||V_2O_5 cells using Zw-Zn(OTf)$_2$-ZnSO$_4$ at various current densities. (b) C-rate performance of Zn||V_2O_5 cells based on different electrolytes. (c) Charging/discharging curves of Zn||V_2O_5 cells using Zw-Zn(OTf)$_2$-ZnSO$_4$ at cycle 1 (0.2 A g^{-1}), cycle 500 (2 A g^{-1}) and cycle 1000 (2 A g^{-1}). (d) Long cycle performance of the Zn||V_2O_5 cells based on different electrolytes. (e) Long cycle performance of the Zn||V_2O_5 cells based on Zw-Zn(OTf)$_2$-ZnSO$_4$ at 0.1A g^{-1} at −20°C, and (f) shows the corresponding charging/discharging curves.

This unique interfacial microenvironment drastically lowers the reduction barrier of these otherwise inert anions, enabling their reductive decomposition during Zn deposition – a process that is thermodynamically prohibited in conventional aqueous electrolytes. Consequently, OTf^- and SO_4^{2-} are reduced in situ to form ZnF_2 and ZnS, respectively, which integrate with the flexible polyzwitterion matrix to form a robust organic–inorganic hybrid SEI. This strategy thus provides a new pathway to harness the reductive decomposition of 'non-electrochemically active' anions for high-performance aqueous zinc batteries, breaking the long-standing limitation that such anions cannot be reduced prior to Zn deposition. The AFM images in Figure 5k–m provide direct evidence of the homogeneous and robust SEI layer formed on the Zn anode based on cycled Zn||Zn cell using Zw-Zn(OTf)$_2$-ZnSO$_4$. The topographic image (Figure 5k) reveals a dense, crack-free surface with a thickness of ~40–80 nm, effectively preventing direct contact between the anode and electrolyte. The 3D modulus mapping (Figure 5l) and 2D plane distribution (Figure 5m) further confirm the hybrid SEI's balanced mechanical properties, where the uniformly dispersed high-modulus inorganic domains and flexible organic phases work together to accommodate volume changes and suppress dendrite growth during cycling.

2.4 | Full Cell Validation and Low Temperature Adaptability

The synergistic effect of zwitterions and $ZnSO_4$ became more pronounced in full-cell configurations. Figure 6a and Figure S14 present galvanostatic charge-discharge profiles of full cells

fabricated with different electrolytes at varying current densities. Rate capabilities shown in Figure 6b demonstrate substantial capacity enhancement across all current densities (1, 2, 4, 5 A g^{-1}) when zwitterions were incorporated, achieving specific capacities of 375, 350, 345, and 300 mAh g^{-1}, respectively. Figure 6c shows the charging/discharing curves of the assembled cell at different cycles, and the long-term cycling performance (Figure 6d) reveals that the Zw-$Zn(OTf)_2$-$ZnSO_4$-based cell maintains superior capacity retention over 1900 cycles, with an average specific capacity of 339 mAh g^{-1} and average Coulombic efficiency of 99.9% (Figure S15). In comparison, cells based on $Zn(OTf)_2$, $Zn(OTf)_2$-$ZnSO_4$, and Zw-$Zn(OTf)_2$ exhibit high average Coulombic efficiencies (e.g., 99.8% for the $Zn(OTf)_2$-$ZnSO_4$-based cell) but suffer from severe overcharging and deliver relatively low average specific discharge capacities of 202, 228, and 275 mAh g^{-1}, respectively. The low-temperature performance of the full cell assembled with the optimal electrolyte was further validated. As shown in Figure 6e, the battery can stably cycle for over 300 cycles at −20°C (the charge/discharge curves are shown in Figure 6f). With the gradual formation of a stable interfacial layer at low temperature, the specific discharge capacity of the battery slowly increases, reaching an average specific capacity of 241 mAh g^{-1} and an average Coulombic efficiency close to 100%. This demonstrates the effectiveness of the electrolyte in facilitating zinc-ion transport kinetics at low temperatures, offering promising potential for battery applications in low-temperature scenarios.

3 | Conclusion

In summary, we have established a polyzwitterionic "ion-sponge" interphase at the zinc anode through in situ polymerization of a polymerizable zwitterion incorporated into a conventional aqueous $Zn(OTf)_2$ electrolyte with $ZnSO_4$. This "ion-sponge" interphase electrostatically enriches anions (OTf^- and SO_4^{2-}) while excluding water and concurrently triggers the formation of a polymer/inorganic hybrid SEI. Unlike conventional approaches relying on uncontrolled decomposition or ex situ coating, our system leverages electric-field-triggered zwitterionic polymerization to generate a flexible polyzwitterion matrix coupled with a mechanically robust inorganic network. Comprehensive theoretical and experimental analyses reveal that the zwitterion weakens Zn^{2+}–H_2O coordination, enhances Zn^{2+} diffusivity at the interface, and suppresses parasitic reactions. Consequently, Zn||Zn symmetric cells deliver outstanding cycling stability exceeding 5500 h, and full cells maintain exceptional capacity retention over 1900 cycles at room temperature as well as stable operation at −20 °C. This work introduces an "ion-sponge" paradigm for interface-targeted zwitterionic engineering, offering a new route for durable, high-rate, and low-temperature aqueous zinc batteries.

Author Contributions

Lei Zhang: conceptualization, methodology, investigation, writing – original draft. **Yunlong Zhang:** conceptualization, formal analysis. **Yixu Wang:** investigation, methodology. **Bo Zhang:** investigation, software, data curation. **Mengyao Li:** data curation. **Lan Yang:** investigation, software. **Qian Wang:** conceptualization, writing – review and editing, supervision. **Haiqi Gao:** conceptualization, supervision, writing – review and editing. **Zhong Jin:** conceptualization, supervision, resources. **Shi Wang:** conceptualization, writing – review and editing.

Acknowledgments

This work was supported by the Key Project of Anhui Provincial Education Department (2024AH051409), the State Key Laboratory of Flexible Electronics Key Task Research Project (ZS030ZR25012), the National Natural Science Foundation of China (62288102, 52533008, U25A20628, 22561160129, 22479074, 22475096, 22408303, 22402146, 22572140), the Equipment Pre-Research and Ministry of Education Joint Fund (8091B02052407), the Fundamental Research Program Key Project of Jiangsu Province (BK20253008), the Science and Technology Major Project of Jiangsu Province (BG2024013), the Scientific and Technological Achievements Transformation Special Fund of Jiangsu Province (BA2023037), the Academic Degree and Postgraduate Education Reforming Project of Jiangsu Province (JGKT24_C001), the Key Core Technology Open Competition Project of Suzhou City (SYG2024122), the Open Research Fund of Suzhou Laboratory (SZLAB-1308-2024-TS005), the Chenzhou National Sustainable Development Agenda Innovation Demonstration Zone Provincial Special Project (2023sfq11, 2025sfq38), the Fundamental Research Funds for the Central Universities and Nanjing University International Collaboration Initiative (020514380354), the National Nature Science Foundaton of NJUPT (NY223079,NY224119), and the Central Government Guidance Fund for Local Sci-Tech Development (ZYYD2025ZY10).

Conflicts of Interest

The author declares no conflicts of interest.

Data Availability Statement

The data that support the findings of this study are available from the corresponding author upon reasonable request.

References

1. X. Zheng, H. Zhu, Z. Wang, et al., "Nanoengineered Aqueous-Hydrotrope Hybrid Liquid Electrolyte Solutions for Efficient Zinc Batteries Across a Wide Temperature Range," *Nature Nanotech* 21 (2026): 95–105, https://doi.org/10.1038/s41565-025-02060-6.

2. L. Zhang, J. Wu, T. Lu, et al., "Improving Zn^{2+} Migration via Designing Multiple Zincophilic Polymer Electrolyte for Advanced Aqueous Zinc Ion Batteries," *Chemical Engineering Journal* 496 (2024): 153815, https://doi.org/10.1016/j.cej.2024.153815.

3. J. Ren, J. Zhang, Y. Chen, et al., "Multiphase Aqueous Soggy Sand Electrolyte for Zinc Metal Batteries Applications at Elevated Temperatures," *Nature Communications* 17 (2025): 309, https://doi.org/10.1038/s41467-025-67020-z.

4. D. Feng, Y. Xie, Y. Jiao, and P. Wu, "Leveraging Cation Effect for Low Temperature Aqueous Zn-Based Batteries," *Nature Communications* 16 (2025): 9254, https://doi.org/10.1038/s41467-025-64278-1.

5. J. Li, A. Azizi, S. Zhou, et al., "Hydrogel Polymer Electrolytes Toward Better Zinc-Ion Batteries: A Comprehensive Review," *eScience* 5 (2025): 100294, https://doi.org/10.1016/j.esci.2024.100294.

6. Y. Guo, Z. Li, and X. Wang, "Crystallinity-Induced Ion Rectification in Polymer/Zn Interphases for Stable Aqueous Zinc Batteries," *Advanced Materials* 37 (2025): 2418354, https://doi.org/10.1002/adma.202418354.

7. Y. Tan, W. Xu, F. Yang, et al., "Dynamic Polyiodide-Trapping and Proton-Capturing Dual-Network Engineering for High-Areal-Capacity, Long-Cycling and High-Temperature Zn—I_2 Batteries," *Advanced Materials* 38 (2026): e22609, https://doi.org/10.1002/adma.202522609.

8. S. Wu, Z. Hu, P. He, L. Ren, J. Huang, and J. Luo, "Crystallographic Engineering of Zn Anodes for Aqueous Batteries," *eScience* 3 (2023): 100120, https://doi.org/10.1016/j.esci.2023.100120.

9. N. Hu, W. Lv, W. Chen, et al., "A Double-Charged Organic Molecule Additive to Customize Electric Double Layer for Super-Stable and Deep-Rechargeable Zn Metal Pouch Batteries," *Advanced Functional Materials* 34 (2024): 2311773, https://doi.org/10.1002/adfm.202311773.

10. W. Lv, J. Tao, D. Huang, et al., "In Situ Constructing Hybrid Solid Electrolyte Interphase and Regulating D-Band Center on Zn Substrate to Enable High-Rate and High-Capacity Zn Metal Anodes," *Advanced Functional Materials* 36 (2026): e13857, https://doi.org/10.1002/adfm.202513857.

11. H. Weng, Y. Zhang, X. Zhou, et al., "Building π–π-Conjugated Molecule Adsorption Layer on Zn Anode for Ultra-Stable Aqueous Zinc-Ion Batteries," *eScience* ahead of print, April 3, (2026): 100580, https://doi.org/10.1016/j.esci.2026.100580.

12. F. Huang, W. Xu, Y. He, D. Li, Y. Tan, and H. He, "Electrolyte Design toward High-Performance Zinc-Iodine Batteries: Progress, Challenges, and Prospects," *Battery Energy* 4 (2025): e70036, https://doi.org/10.1002/bte2.20250017.

13. M. Zhao, Y. Lv, Y. Xu, H. Yang, Z. Bo, and J. Lu, "Ordered Zinc Electrodeposition From Single-Crystal Units to Polycrystalline Stacking Within Solid-Electrolyte Interphase in Battery Anodes," *Nature Communications* 16 (2025): 2843, https://doi.org/10.1038/s41467-025-58063-3.

14. H. Wang, G. Li, J. Fu, et al., "Regulating Zinc Nucleation and Growth With Low-Surface-Tension Electrolytes for Practical Aqueous Zinc Metal Batteries," *Nature Communications* 17 (2026): 1690, https://doi.org/10.1038/s41467-026-68393-5.

15. X. Wu, Y. Dai, N. W. Li, X. C. Chen, and L. Yu, "Recent Progress in Ionic Liquid-Based Electrolytes for Nonaqueous and Aqueous Metal Batteries," *eScience* 4 (2024): 100173, https://doi.org/10.1016/j.esci.2023.100173.

16. S. Wang, J. Li, B. Yang, et al., "Unlocking the Potential of Aqueous Zinc-Ion Batteries: Hybrid SEI Construction Through Bifunctional Regulator-Assisted Electrolyte Engineering," *Nano Letters* 25 (2025): 5406–5414, https://doi.org/10.1021/acs.nanolett.5c00533.

17. T. Lu, S. Wang, C. Liu, et al., "Inverse Solvation Configuration Induced by Organic Small-Molecule Spatially-Confined Coordination Enables Highly Reversible Zinc Batteries," *Advanced Functional Materials* 36 (2025): e23416, https://doi.org/10.1002/adfm.202523416.

18. C. Yang, P. Woottapanit, S. Geng, et al., "A Multifunctional Quasi-Solid-State Polymer Electrolyte With Highly Selective Ion Highways for Practical Zinc Ion Batteries," *Nature Communications* 16 (2025): 183, https://doi.org/10.1038/s41467-024-55656-2.

19. T. Shen, Z.-J. Chen, Y. Yang, et al., "Thinner-Than-Paper and Broad-Temperature-Adaptive Zinc-Iodine Batteries Enabled by Nanophase Separated Deep-Eutectic Hydrogel Electrolytes," *Nature Communications* 17 (2026): 4827, https://doi.org/10.1038/s41467-026-71312-3.

20. S. Wang, X. Wu, C. Liu, et al., "Hydrogen Bond-induced Elastic Polyzwitterion Electrolytes Constructed by Mussel-Inspired Autopolymerization for Zinc-Ion Battery," *Science China Chemistry* 67 (2024): 3438–3449, https://doi.org/10.1007/s11426-024-2133-1.

21. K. Xie, K. Ren, Q. Wang, et al., "In Situ Construction of Zinc-Rich Polymeric Solid–Electrolyte Interface for High-Performance Zinc Anode," *eScience* 3 (2023): 100153, https://doi.org/10.1016/j.esci.2023.100153.

22. L. Zhang, J. Xiao, X. Xiao, et al., "Molecular Engineering of Self-Assembled Monolayers for Highly Utilized Zn Anodes," *eScience* 4 (2024): 100205, https://doi.org/10.1016/j.esci.2023.100205.

23. B. Li, B. Zhang, X. Bai, et al., "A Dynamic Self-Healing Protective Layer Enabling Stable Zinc Ion Batteries Through Strong Zn-S Affinity and Intramolecular Hydrogen Bonding," *Angewandte Chemie International Edition* 137 (2025): e202503345, https://doi.org/10.1002/ange.202503345.

24. R. Chen, W. Zhang, C. Guan, et al., "Rational Design of an In-Situ Polymer-Inorganic Hybrid Solid Electrolyte Interphase for Realising Stable Zn Metal Anode Under Harsh Conditions," *Angewandte Chemie International Edition* 136 (2024): e202401987, https://doi.org/10.1002/ange.202401987.

25. X. Liu, Y. Zhang, L. Wang, et al., "Highly Reversible Dendrite-Free Zinc Anode Enabled by a Bilayered Inorganic-Metal Interface Layer," *ACS Nano* 18 (2024): 35325–35335, https://doi.org/10.1021/acsnano.4c11486.

26. P. Xiao, Y. Wu, K. Liu, et al., "An Ultrathin Inorganic Molecular Crystal Interfacial Layer for Stable Zn Anode," *Angewandte Chemie International Edition* 62 (2023): e202309765, https://doi.org/10.1002/anie.202309765.

27. T. Zhao, Y. Zheng, S. Jiang, M. Li, and K. Sun, "Interface Regulation Mechanisms and Research Progress of Organic Small-Molecule Additives in Aqueous Zinc-Ion Batteries," *Energy Storage Materials* 81 (2025): 104483, https://doi.org/10.1016/j.ensm.2025.104483.

28. P. Xue, C. Guo, W. Gong, et al., "Multifunctional Polymer Interphase With Fast Kinetics for Ultrahigh-Rate Zn Metal Anode," *Angewandte Chemie International Edition* 64 (2025): e202500295, https://doi.org/10.1002/anie.202500295.

29. M. Zhu, J. Hu, Q. Lu, et al., "A Patternable and In Situ Formed Polymeric Zinc Blanket for a Reversible Zinc Anode in a Skin-Mountable Microbattery," *Advanced Materials* 33 (2021): 2007497, https://doi.org/10.1002/adma.202007497.

30. R. Zhao, Z. Feng, R. Kuang, et al., "UV-Polymerized Zincophilic Ion-Enhanced Interfacial Layer with High Ion Transference Number for Ultrastable Zn Metal Anodes," *Carbon Neutralization* 4 (2025): e194, https://doi.org/10.1002/cnl2.194.

31. A. M. Paswan, V. S. Thakur, S. Banerjee, and C. R. Raj, "Electrochemical Engineering of Anode With Zincophilic Polymer Interface for Reversible Zinc Battery," *Advanced Functional Materials* 35 (2025): 2412370, https://doi.org/10.1002/adfm.202412370.

32. D. Luo, B. Niu, P. Du, et al., "Pre-Established Ion Transport Pathways through Electrolyte Initiator for High-Efficiency Polymer Interface Enabling Ultra-Stable Aqueous Zinc-Metal Anodes," *Advanced Materials* 37 (2025): 2418741, https://doi.org/10.1002/adma.202418741.

33. Y. Luo, L. Zhao, D. Yin, et al., "Recent Advances in Polymer Interlayers for Zinc Metal Anode Protection-a Mini-Review," *ChemElectroChem* 12 (2025): e202400692, https://doi.org/10.1002/celc.202400692.

34. A. Chen, C. Zhao, J. Gao, et al., "Multifunctional SEI-Like Structure Coating Stabilizing Zn Anodes at a Large Current and Capacity," *Energy & Environmental Science* 16 (2023): 275–284, https://doi.org/10.1039/D2EE02931F.

35. W. Zhang and G. He, "Solid-Electrolyte Interphase Chemistries Towards High-Performance Aqueous Zinc Metal Batteries," *Angewandte Chemie International Edition* 62 (2023): e202218466, https://doi.org/10.1002/anie.202218466.

36. Q. Wang, Z. Zhang, Z. Hu, et al., "Manipulating Interphase Chemistry for Aqueous Zn Stabilization: The Role of Supersaturation," *Angewandte Chemie International Edition* 64 (2025): e202420772, https://doi.org/10.1002/anie.202420772.

37. G. Li, Z. Zhao, S. Zhang, et al., "A Biocompatible Electrolyte Enables Highly Reversible Zn Anode for Zinc Ion Battery," *Nature Communications* 14 (2023): 6526, https://doi.org/10.1038/s41467-023-42333-z.

Supporting Information

Additional supporting information can be found online in the Supporting Information section.

Supporting File: anie74069-sup-0001-SuppMat.docx.